ADVANCED MATERIALS
www.advmat.de

Check for updates

Precise Control of Perovskite Crystallization Kinetics via Sequential A-Site Doping

Minchao Qin, Haibo Xue, Hengkai Zhang, Hanlin Hu, Kuan Liu, Yuhao Li, Zhaotong Qin, Junjie Ma, Hepeng Zhu, Keyou Yan, Guojia Fang, Gang Li, U-Ser Jeng, Geert Brocks, Shuxia Tao, and Xinhui Lu**

Two-step-fabricated $FAPbI_3$-based perovskites have attracted increasing attention because of their excellent film quality and reproducibility. However, the underlying film formation mechanism remains mysterious. Here, the crystallization kinetics of a benchmark $FAPbI_3$-based perovskite film with sequential A-site doping of Cs^+ and GA^+ is revealed by in situ X-ray scattering and first-principles calculations. Incorporating Cs^+ in the first step induces an alternative pathway from δ-$CsPbI_3$ to perovskite α-phase, which is energetically more favorable than the conventional pathways from PbI_2. However, pinholes are formed due to the nonuniform nucleation with sparse δ-$CsPbI_3$ crystals. Fortunately, incorporating GA^+ in the second step can not only promote the phase transition from δ-$CsPbI_3$ to the perovskite α-phase, but also eliminate pinholes via Ostwald ripening and enhanced grain boundary migration, thus boosting efficiencies of perovskite solar cells over 23%. This work demonstrates the unprecedented advantage of the two-step process over the one-step process, allowing a precise control of the perovskite crystallization kinetics by decoupling the crystal nucleation and growth process.

Perovskite solar cells (PSCs) have reached a striking power conversion efficiency (PCE) over 25% in recent years.[1] One essential aspect to boost the PCE is to optimize the perovskite film deposition process to achieve desired morphology and microstructure.[2–6] Most of the high-efficiency PSCs were produced by either one-step or two-step fabrication methods. The very first $MAPbI_3$-based PSC was fabricated via a one-step spin-coating process developed by Kojima et al. in 2009.[7] However, the one-step fabricated perovskite film typically exhibited a dendritic morphology with poor coverage. To address the morphology issue, a two-step spin-coating process was developed by Xiao et al.[8] and Im et al.[9] in 2014, which consisted of sequential depositions of an inorganic PbI_2 layer and an organic salt MAI. This two-step method gave rise to compact and pinhole-free $MAPbI_3$ perovskite films, significantly increasing the efficiency of MA-based PSCs to ≈17%.[9] In 2015, the record PCE received another boost through the development of a simpler antisolvent-assisted one-step method, which could form a very uniform perovskite thin film by promoting the crystallization process.[4,10] Meanwhile, MA cations were replaced by $CH(NH_2)_2^+$ (FA) cations to improve the light

M. Qin, Y. Li, Z. Qin, Prof. X. Lu
Department of Physics
The Chinese University of Hong Kong
Shatin 999077, Hong Kong
E-mail: xinhui.lu@cuhk.edu.hk

H. Xue, Prof. G. Brocks, Prof. S. Tao
Materials Simulation and Modelling and Center for Computational Energy Research
Department of Applied Physics
Eindhoven University of Technology
P.O. Box 513, Eindhoven 5600MB, The Netherlands
E-mail: s.x.tao@tue.nl

H. Zhang, Dr. K. Liu, Prof. G. Li
Department of Electronic and Information Engineering
The Hong Kong Polytechnic University
Kowloon 999077, Hong Kong

Dr. H. Hu
Hoffmann Institute of Advanced Materials
Shenzhen Polytechnic
7098 Liuxian Boulevard, Shenzhen 518055, P. R. China

Dr. J. Ma, Prof. G. Fang
Key Lab of Artificial Micro- and Nano-Structures of Ministry of Education of China
School of Physics and Technology
Wuhan University
Wuhan 430072, P. R. China

H. Zhu, Prof. K. Yan
School of Environment and Energy
State Key Laboratory of Luminescent Materials and Devices
National Engineering Laboratory for VOCs Pollution Control Technology and Equipment
South China University of Technology
Guangzhou 510006, P. R. China

Dr. U.-S. Jeng
National Synchrotron Radiation Research Center
Hsinchu Science Park, Hsinchu 30076, Taiwan

Dr. U.-S. Jeng
Department of Chemical Engineering
National Tsing Hua University
Hsinchu 30013, Taiwan

The ORCID identification number(s) for the author(s) of this article can be found under https://doi.org/10.1002/adma.202004630.

DOI: 10.1002/adma.202004630

 © 2020 Wiley-VCH GmbH

absorption and thermal stability of devices, which resulted in an efficiency of 19% for $FAPbI_3$-based PSCs obtained with the one-step antisolvent spin-coating method.[5,11] Besides, other inorganic or organic A-site cations (e.g., Cs^+, Rb^+, guanidinium (GA^+)) with different ionic radii were doped into the perovskites to enhance the phase crystallinity and stability as well as to passivate defects, further pushing the PCEs to over 22% with the one-step antisolvent method.[12–14] Recently, the two-step spin-coating process was modified by You and co-workers to fabricate $FAPbI_3$-based PSCs as well, delivering a record high efficiency of 23.32% due to reduced defect density and nonradiative recombination.[15,16] However, there are still very limited studies on the A-site engineering and the fundamental film formation mechanism for the two-step spin-coating process.

To understand the perovskite film formation mechanism, in situ grazing-incidence wide-angle X-ray scattering (GIWAXS) characterization is usually employed.[17] For the one-step process, there are fruitful and interesting in situ studies for the film being formed under thermal annealing,[18] spin-coating,[19,20] blade coating,[21] and slot-die coating.[22] It is found that the crystal growth kinetics of the one-step process is very complex and time sensitive, as it often involves the dynamic competition between multiple phases and intermediate phases.[23] This makes the one-step process intricate to control, highly relying on fabrication experiences and skills.[24] In comparison to the one-step process, the two-step method has demonstrated a wider tunability and a better control over the crystallization of perovskites,[25] which could involve a totally different crystallization process and the underlying crystal growth mechanism. Jiang et al. fixed the thickness of PbI_2 layer in the first step and tuned the amount of organic salt to optimize the residual PbI_2 contents in the perovskite layer, finally achieving a high PCE of 21.6%.[26] Meng et al. employed in situ GIWAXS measurements to investigate the annealing process of the PbI_2 and the perovskite, and found that adding ions of Br^-, Cl^- and MA^+ could accelerate the perovskite crystallization speed and modulate crystal grain orientations.[27] However, in situ study of the whole two-step process, especially during the two spin-coating steps, has not been reported.

In this work, we demonstrate a precise control of perovskite film formation in a two-step spin-coating process by performing sequential A-site doping of Cs^+ and GA^+ cations in $FAPbI_3$-based perovskites. The growth of the films involves manifold crystallization pathways and thereby leads to distinct film morphologies, as unveiled by in situ GIWAXS measurements. It is found that in the undoped film, the two-step process can effectively decouple the crystal nucleation and crystal growth, as the hexagonal PbI_2 formed in the first step essentially gives the nucleation sites for further growth of the perovskite α-phase in the second step. Remarkably, the doping of Cs^+ cations induces the formation of the δ-$CsPbI_3$ phase and restrains the crystallization of PbI_2. Density functional theory (DFT) results indicate that the transition to the α-phase preferentially initiates from the δ-$CsPbI_3$ phase instead of PbI_2, as the reaction enthalpy in a Cs-rich environment is relatively lower. Therefore, the δ-$CsPbI_3$ phase offers an alternative phase transition pathway to the perovskite α-phase, while the sparse nucleation sites of δ-$CsPbI_3$ give rise to the growth of large grains but many pinholes caused by the nonuniform nucleation. Fortunately, this problem can be solved by doping GA^+ cations in the second step, which noticeably accelerates the crystal growth speed and results in large grains free of voids via Ostwald ripening and enhanced grain boundary migration. This observation is rationalized by DFT results, which show that GA^+ balances the bonding stress caused by the Cs^+ doping, through an increased bonding strength with Pb–I octahedral frameworks. Using the perovskites fabricated through the sequential doping of Cs^+ and GA^+, device efficiencies over 23% were achieved, owing to the improved morphology, enhanced crystallinity, and reduced defects. Our work reveals an unprecedented advantage of the two-step process over the one-step process: the two-step process decouples nucleation and crystal growth and offers sequential doping handles to a precise control of perovskite film growth toward high-efficiency devices.

Figure 1a illustrates the two-step process we adopt from previous reports[16,26] to fabricate $FAPbI_3$-based perovskite films. In the first step, a PbI_2 layer is deposited by spin-coating a PbI_2 precursor solution, followed by thermal annealing at 70 °C. In the second step, an isopropyl alcohol (IPA) solution containing organic salts (formamidinium iodide (FAI), methylammonium bromide (MABr), and methylammonium chloride (MACl)) is dropped on top of the film formed in the first step, which creates a perovskite film through the interdiffusion of PbI_2 and organic salts. Here, the mass ratio of FAI:MABr:MACl is 60 mg:6 mg:6 mg. MABr is introduced to improve the perovskite phase stability, while Cl assists the perovskite crystal growth as an intermediate element.[6,25] The sequential doping of Cs^+ and GA^+ is achieved by adding CsI and guanidinium iodide (GAI) into the precursor solutions for the first and the second step, respectively. In situ GIWAXS characterization was performed at the synchrotron beamline 23A1, National Synchrotron Radiation Research Center (NSRRC) to monitor the real-time phase evolution from precursor to perovskite during the two-step process (Figure 1b). The X-ray incidence angle was set to 2°. Based on the estimated X-ray penetration depth (Figure S1, Supporting Information), a full penetration of the film is ensured at this incident angle.

We first examined the phase evolution in the first step by plotting the false-color GIWAXS intensity maps versus wave number q (y-axis) and frame numbers (x-axis) during spin-coating (**Figure 2**a) and the subsequent annealing (Figure 2b) processes of the PbI_2 precursor solution without Cs^+. The corresponding intensity profiles, averaged over polar angles, are summarized in Figure S2 in the Supporting Information. Note that the exposure time for each frame was 1 s during spinning and 2 s during annealing, since the former usually involves relatively faster dynamics. The peaks located at $q \approx 1.9$ and 2.4 $Å^{-1}$ are originated from the fluorine-doped tin oxide (FTO) substrate. Upon the launch of the spinning, a broad scattering peak centered at ≈0.5 $Å^{-1}$ can be observed, which is associated with the precursor solution.[19,22] After ≈15 s of spinning, a scattering peak, corresponding to the metastable PbI_2-DMF-DMSO

Prof. G. Brocks
Computational Materials Science
Faculty of Science and Technology and MESA+ Institute for Nanotechnology
University of Twente
P.O. Box 217, Enschede 7500AE, The Netherlands

 © 2020 Wiley-VCH GmbH

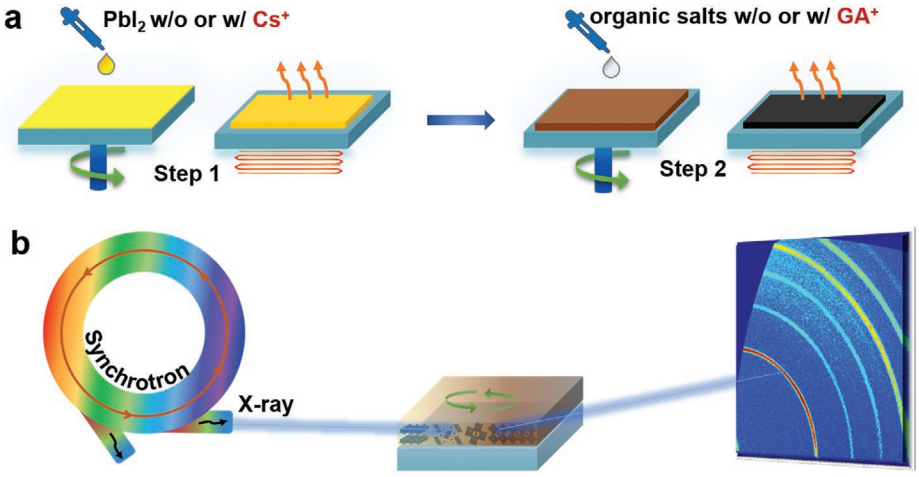

Figure 1. Schematics of the two-step fabrication procedure and synchrotron-based in situ GIWAXS measurements. a) Two-step fabrication process of perovskite films doped with Cs^+ and GA^+ during the first and second step, respectively. b) A sketch map of synchrotron-based in situ GIWAXS measurements.

intermediate phase,[11,28] emerges at $q \approx 0.49$ Å^{-1}, which then decreases slowly along with the spinning process (Figure 2c). The crystalline PbI_2 phase does not appear in the course of spinning until the film is annealed at 70 °C. After having been annealed for ≈40 s, the PbI_2-DMF-DMSO intermediate phase vanishes, accompanied with the emergence of the (001) hexagonal PbI_2 phase peak at 0.9 Å^{-1},[29] as shown in Figure 2b,c. The peak area of PbI_2 keeps changing incrementally and becomes stable after 120 s.

Interestingly, the film formed from the PbI_2 precursor solution with 5% Cs^+, undergoes a distinct crystallization pathway. A new crystalline phase was detected after ≈45 s of spinning (Figure 2d), indicated by the simultaneous appearance of scattering peaks at 0.70, 1.55, 1.83, and 2.08 Å^{-1}, suggesting the emergence of the δ-$CsPbI_3$ phase (Figure S2c, Supporting Information).[30] It indicates that the δ-$CsPbI_3$ phase can be formed at a much lower temperature than the α-phase temperature due to the lower formation energy,[31] which is also confirmed by X-ray diffraction (XRD) data (Figure S3, Supporting Information). The peak at 0.70 Å^{-1} is chosen to represent the δ-$CsPbI_3$ phase in the rest of the work. Its peak area keeps increasing until it is saturated after ≈80 s of spinning. In the meantime, the hexagonal PbI_2 phase peak appears at 0.90 Å^{-1} as early as ≈50 s and remains at a low intensity during the spinning process. When

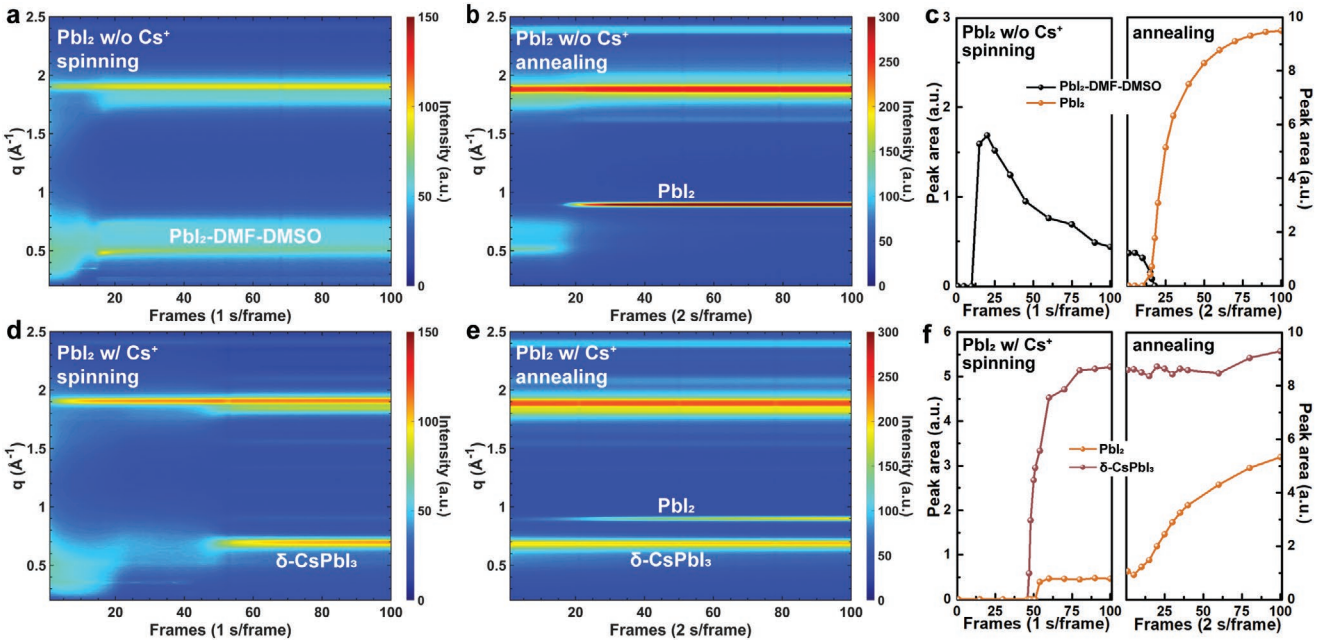

Figure 2. Time-resolved GIWAXS profile analysis during the first step. a,b) The false-color intensity maps versus wave number q and frame numbers for PbI_2 without Cs^+ during the spinning (a) and annealing (b) processes. c) The corresponding time evolutions of peak areas of the PbI_2-DMF-DMSO intermediate phase and the PbI_2 phase. d,e) The false-color intensity maps for the film with 5% Cs^+ during the spinning (d) and annealing (e) processes, and f) the corresponding time evolutions of the peak areas of the PbI_2 and δ-$CsPbI_3$ phases.

© 2020 Wiley-VCH GmbH

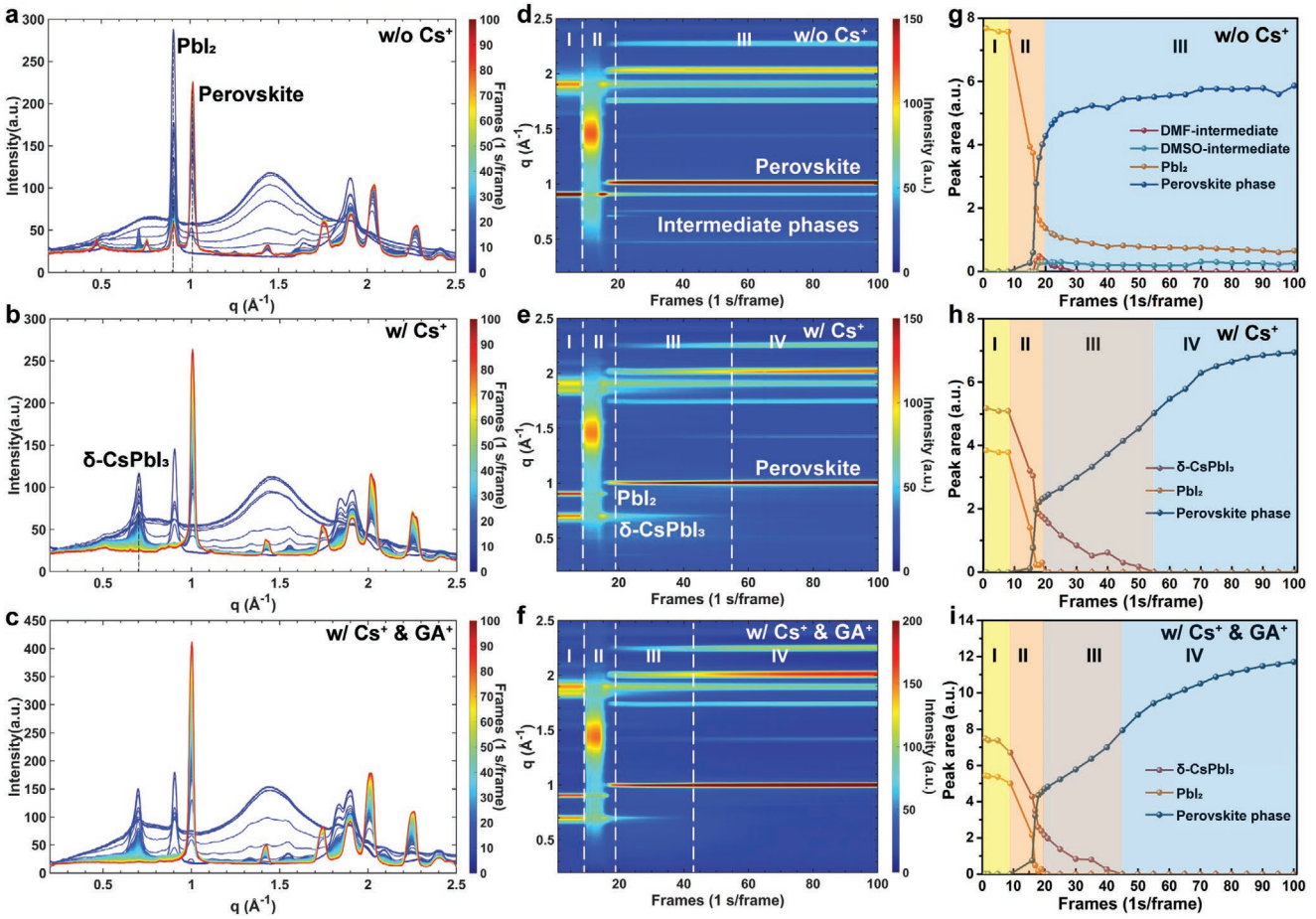

Figure 3. Perovskite film formation analysis during the second step. a–c) The GIWAXS intensity profiles for perovskites without doping (a), with 5% Cs^+ (b), and with Cs^+ and GA^+ (c), respectively. d–f) The corresponding false-color intensity maps versus q and frame numbers and g–i) the time evolutions of peak areas of intermediate, PbI_2, δ-$CsPbI_3$, and perovskite phases.

the film is further annealed at 70 °C (Figure 2e), the PbI_2 phase experiences a much larger increase than that of the δ-$CsPbI_3$ phase, implying that the crystal growth of PbI_2 is more likely to be thermally activated. Nevertheless, the resultant peak area after annealing is still smaller than that of the δ-$CsPbI_3$ phase. It is worth mentioning that with only 5% of Cs^+, the peak area of the hexagonal PbI_2 phase is much lower than that in the film without Cs^+, suggesting that the formation of δ-$CsPbI_3$ phase restrains the crystallization of PbI_2. The 2D GIWAXS patterns and the corresponding intensity profiles of the resultant films are shown in Figure S4 in the Supporting Information. Besides crystallization pathways, the initial state of the PbI_2 solution could influence the resultant PbI_2 film.[32] We measured the absorption spectra of the PbI_2 solutions without and with Cs^+. They both present similar absorption edges and no additional absorption peak is observed after incorporating Cs^+ (Figure S5, Supporting Information), suggesting that the initial state of PbI_2 does not alter significantly with Cs^+. In short, we conclude that the incorporation of Cs^+ in PbI_2 leads to the coexistence of dominant δ-$CsPbI_3$ and suppressed PbI_2 phases. It offers alternative phase transition pathways to the perovskite phase as well as relatively sparse nucleation centers for further crystal growth in the second step.

Setting off from different phase compositions formed with and without Cs^+ in the first step, the phase evolution pathways diverge noticeably in the second step (**Figure 3**). By dropping the IPA solution of FAI, MABr, and MACl on the film without Cs^+, three stages can be identified. The initial stage (stage I) consists of the hexagonal PbI_2 phase formed in the first step, indicated by the sharp scattering peak at $q \approx 0.9$ Å^{-1} (Figure 3a). The phase transition stage (stage II) is triggered by dropping the organic salt solution at the 9th s, leading to a broad scattering peak at $q \approx 1.45$ Å^{-1}. Along with the vanishing of the solution peak, the PbI_2 peak quickly drops to a low intensity, followed by a sharp rise of the perovskite α-phase peak at $q \approx 1.0$ Å^{-1}. The whole process finishes within 12 s, indicating a fast phase transition as a result of prompt interdiffusion between PbI_2 and organic salts. Simultaneously, a DMF intermediate phase[33] and a DMSO intermediate phase[34] are detected at $q \approx 0.70$ Å^{-1} and $q \approx 0.75$ Å^{-1}, respectively. Entering stage III, the perovskite phase further grows and quickly reaches saturation at the 30th s, which is accompanied by the disappearance of the DMF intermediate phase. Then, the perovskite phase, the remnant PbI_2, and the DMSO intermediate phase coexist with barely changed peak area, indicating the cessation of further crystal growth.

© 2020 Wiley-VCH GmbH

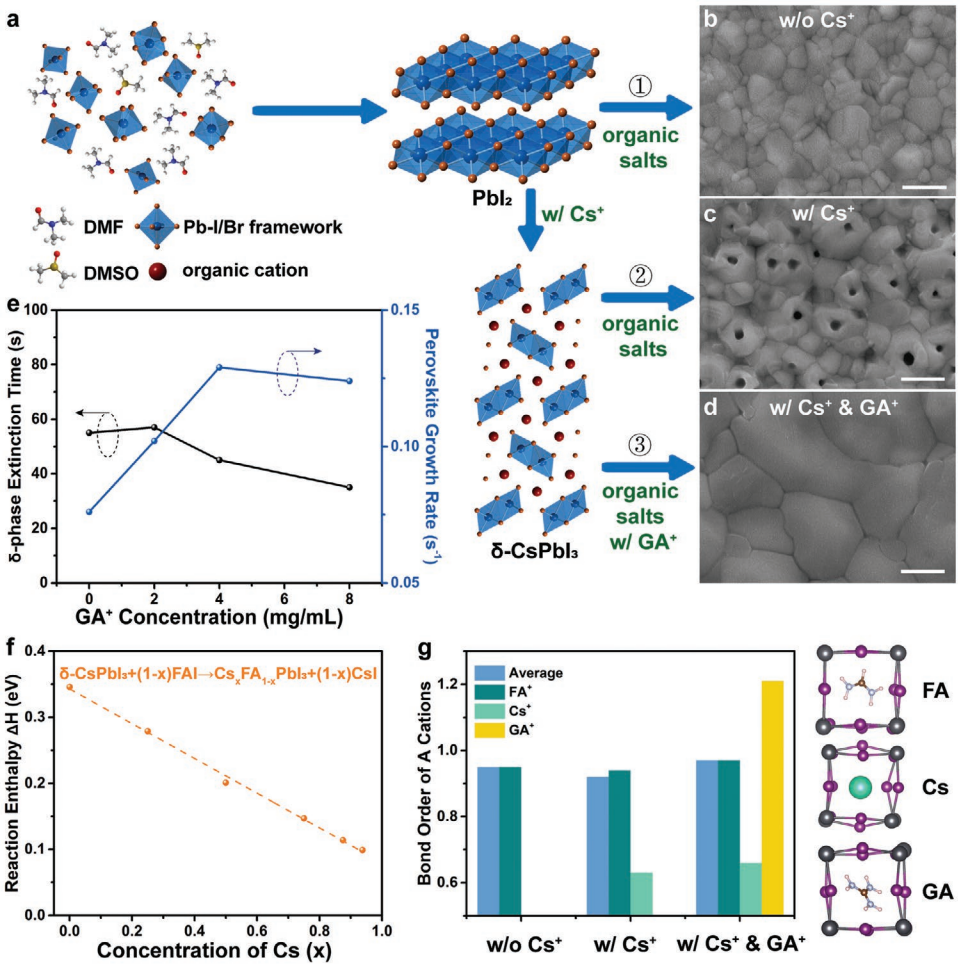

Figure 4. The roles of Cs^+ and GA^+ in the crystallization process. a) Schematics of three phase transition pathways from PbI_2 precursor to perovskites without Cs^+, with Cs^+, and with Cs^+ & GA^+, respectively. b–d) Top-view SEM images of perovskite films without Cs^+ doping (b), with 5% Cs^+ (c), and with Cs^+ & GA^+ (d), respectively. The scale bars are 500 nm. e) δ-$CsPbI_3$ phase extinction time and perovskite growth rate with different concentrations of GA^+ extracted from in situ GIWAXS results. f) The calculated reaction enthalpy of the reaction that forms 3D perovskite $FA_{1-x}Cs_xPbI_3$ from δ-$CsPbI_3$. g) The total bond order between A cations (FA^+, Cs^+, GA^+) and the surrounding Pb–I inorganic framework in $FAPb(I_{15/16}Br_{1/16})_3$, $(Cs_{1/16}FA_{15/16})Pb(I_{15/16}Br_{1/16})_3$, and $(GA_{1/16}Cs_{1/16}FA_{14/16})Pb(I_{15/16}Br_{1/16})_3$ structures, and the corresponding sketches of Pb–I frameworks containing FA^+, Cs^+, and GA^+, respectively. The bond order of FA^+ is the average value of all FA^+ cations, and the average bond order is that of all FA^+, Cs^+, and GA^+ cations.

In contrast, four stages can be identified for the film with 5% Cs^+ as shown in Figure 3b,e–h. The initial stage (stage I) contains PbI_2 and δ-$CsPbI_3$ phases formed in the first deposition step. After the organic salt solution is dropped on the film at the 9th s to launch stage II, both the peak areas of PbI_2 and δ-$CsPbI_3$ phases experience a quick drop and the perovskite phase is formed concomitantly (Figure 3h). The PbI_2 peak decreases to zero with a decrease rate of 0.316 s^{-1}, which is a little smaller than that in the film without Cs^+ (0.518 s^{-1}), setting a similar end point for stage II. Noticeably, the transition from the δ-$CsPbI_3$ phase to the perovskite phase continues in stage III at a much slower transition rate of 0.047 s^{-1}. Stage III ends at the ≈55th s, signified by the disappearance of the δ-$CsPbI_3$-phase peak. The perovskite α-phase peak further intensifies for another 30 s in stage IV until saturation. Note that adding 5% or more Cs^+ is required to activate the new phase transition pathway from the δ-$CsPbI_3$ to the perovskite phase. For a film with a lower Cs^+ concentration, such as 2% Cs^+, the crystallization process is similar to that without Cs^+, as shown in Figure S6 in the Supporting Information.

When we introduce GA^+ cations (4 mg mL^{-1}) in the organic salt solution that is dropped onto the film with 5% Cs^+, a similar four-stage crystallization process is observed (Figure 3c,f,i). Intriguingly, stage III ends earlier at the 45th s, as the phase transition rate is calculated to be 0.086 s^{-1}, which is faster than that in the 5% Cs^+ doped film without GA^+ (0.047 s^{-1}), indicating that GA^+ induces an accelerated phase transition from δ-$CsPbI_3$ to the perovskite phase.

Based on the in situ GIWAXS results, three crystallization pathways are identified (**Figure 4**a): 1) a direct phase transition from PbI_2 to perovskites without doping, 2) an alternative phase transition from δ-$CsPbI_3$ to perovskites with Cs^+, and 3) a relatively faster phase transition from δ-$CsPbI_3$ to perovskites with Cs^+ & GA^+. Interestingly, these three different crystallization pathways result in distinct surface morphologies of the final perovskite films according to scanning electron

© 2020 Wiley-VCH GmbH

microscopy (SEM) measurements. The perovskite film without doping (Figure 4b) shows a typical compact microstructure with an averaged grain size of ≈300 nm. The perovskite film with 5% Cs^+ (Figure 4c) presents slightly larger crystalline grains but numerous pinholes. It is found that the pinholes are formed when the Cs^+ concentration is relatively high (≥5%) (Figure S7, Supporting Information), while a lower Cs^+ concentration such as 2% cannot induce the formation of δ-$CsPbI_3$.

In contrast, a more uniform film with significantly enlarged grain sizes is obtained with the incorporation of GA^+ as shown in Figure 4d. The pinholes are gradually eliminated with the increment of the GA^+ concentration (Figure S8, Supporting Information). It is noted that the PbI_2-DMF-DMSO intermediate phases may help eliminate the pinholes in the film without Cs^+.[32] However, it cannot explain the distinct morphology for the films with Cs^+ and with Cs^+ & GA^+, since both of them did not exhibit intermediate phases during the crystallization (Figure 3e,f). Therefore, it is evident that the pinholes formed in the film with Cs^+ are prevented by the incorporation of the GA^+. The perovskite crystallization processes with different GA^+ concentrations were further scrutinized by in situ GIWAXS measurements, as shown in Figure S9 in the Supporting Information. The extinction time of the δ-$CsPbI_3$ phase is shortened and the perovskite growth rate increases with the increase of GA^+ concentration, as summarized in Figure 4e. The distribution statistics of the crystal grain sizes for the perovskite films without doping, with Cs^+, and with Cs^+ & GA^+ are shown in Figure S10 in the Supporting Information. The average grain size for the film with Cs^+ & GA^+ is about 1 µm.

DFT calculations were performed for further understanding of the role of Cs^+ and GA^+ in the crystallization process. Two reactions are defined to simulate the phase transitions to perovskite phases, corresponding to the situations without and with Cs^+, respectively:

$$PbI_2 + FAI \rightarrow FAPbI_3 \tag{1}$$

$$\delta\text{-}CsPbI_3 + (1-x)FAI \rightarrow FA_{1-x}Cs_xPbI_3 + (1-x)CsI \tag{2}$$

where x is the concentration of Cs in the $FA_{1-x}Cs_xPbI_3$ perovskite. It is noted that CsI is produced by reaction 2 and surrounded by PbI_2, so it is likely to be followed up immediately by the reaction

$$CsI + PbI_2 \rightarrow \delta\text{-C-sPbI}_3 \tag{3}$$

which creates new δ-$CsPbI_3$ as nucleation sites, where crystal growth reaction 2 can proceed.

To calculate the reaction enthalpies of these reactions, we choose a relatively large (2 × 2 × 4) $FAPbI_3$ supercell, so that multiple concentrations of the Cs^+ in the $FA_{1-x}Cs_xPbI_3$ perovskite can be modelled by replacing FA^+ with different numbers of Cs^+. Note that in the experiment the perovskite film also contains a minor amount of MA^+ and Br^-.[16] These are not included in the calculation of reaction enthalpies, however, in order to be able to focus on the role of Cs^+ cations. The calculated reaction enthalpies (ΔH) of reaction 2 are shown in Figure 4f. For reaction 2, the ΔH decreases linearly with the increase of the Cs^+ concentration, becoming even lower than that of reaction 1 (ΔH = 0.17 eV). Based on Brønsted–Evans–Polanyi (BEP) principle,[35] the lower reaction energies correspond to smaller activation barriers. This implies that at the beginning of the second step, the reaction prefers to initiate at the δ-$CsPbI_3$ phase crystallites, attracting FA^+ to form the perovskite phase. Then the generated CsI reacts with the surrounding PbI_2 rapidly to produce new δ-$CsPbI_3$ (reaction 3) due to a much lower ΔH of −0.18 eV, giving rise to sparse nucleation centers for further crystal growth. With the gradual consumption of δ-$CsPbI_3$ by reaction 2 and the consumption of PbI_2 by reaction 3, the ratio of δ-$CsPbI_3$ to FAI would decrease, ultimately halting the reaction. The decelerated crystal growth at stage III (Figure 3h) is consistent with a scenario where the conversion of the δ-$CsPbI_3$ to the perovskite by reaction 2 is slowing down.

Moreover, as analyzed above, although the δ-$CsPbI_3$ is important for the overall crystal growth processes, it is involved as an intermediate species, namely, nucleation sites, which is consumed in reaction 2 ultimately. Therefore, δ-$CsPbI_3$ is absent in the final perovskite film (Figure 3h). It is also worth mentioning that, although the reaction enthalpies of reaction 2 are slightly positive (Figure 4f), such reactions are typically driven by entropy of mixing.[36]

The addition of GA^+ cations accelerates the conversion of δ-$CsPbI_3$ to the perovskite (Figure 3i). We estimate the mixing enthalpy (ΔH_{mix}) for the ternary mixing of Cs^+, GA^+, and FA^+ in the perovskite phase relative to the binary compounds by

$$\Delta H_{mix} = E\left[GA_xCs_xFA_{1-2x}Pb(I_{1-x}Br_x)_3\right] + E\left[FAPb(I_{1-x}Br_x)_3\right] - E\left[Cs_xFA_{1-x}Pb(I_{1-x}Br_x)_3\right] - E\left[GA_xFA_{1-x}Pb(I_{1-x}Br_x)_3\right] \tag{4}$$

where E[...] are the DFT calculated total energies of the corresponding compounds per supercell (see calculation methods for details). The structures involved in this calculation are illustrated in Figure S11 in the Supporting Information. According to the energy-dispersive X-ray (EDX) analysis, the experimental concentration of Br^- is ≈5% in three types of perovskite films while the content of Cs^+ in the perovskite films with Cs^+ is in the range of 5.5–6.0%, as summarized in Table S1 in the Supporting Information. Regarding the concentration of GA^+, it is calculated with the XRD peak shift in Figure S12 in the Supporting Information.[37] As summarized in Table S2 in the Supporting Information, the ratio of GA^+ in the film is ≈6.47% when the concentration of GAI in the IPA solution is 8 mg mL^{-1}. Therefore, we have used a close value of $x = \frac{1}{16}$ (6.25%) to simulate the experimental concentrations of Br^-, Cs^+, and GA^+. The ΔH_{mix} is calculated to be − 0.16 eV. Such a negative mixing enthalpy indicates that the ternary (GACsFA) phase is the most favorable phase. This indicates that reaction 2 can proceed faster at the presence of GA^+ when a ternary compound is formed.

The above analysis is further supported by a chemical bonding analysis. The calculated total bond order, a measure of the covalent bond strength between A cations (FA^+, Cs^+, GA^+) and the surrounding Pb–I inorganic framework, is given in Figure 4g. It indicates that doping Cs^+ introduces a locally weak interaction, which is about one-third smaller than that

© 2020 Wiley-VCH GmbH

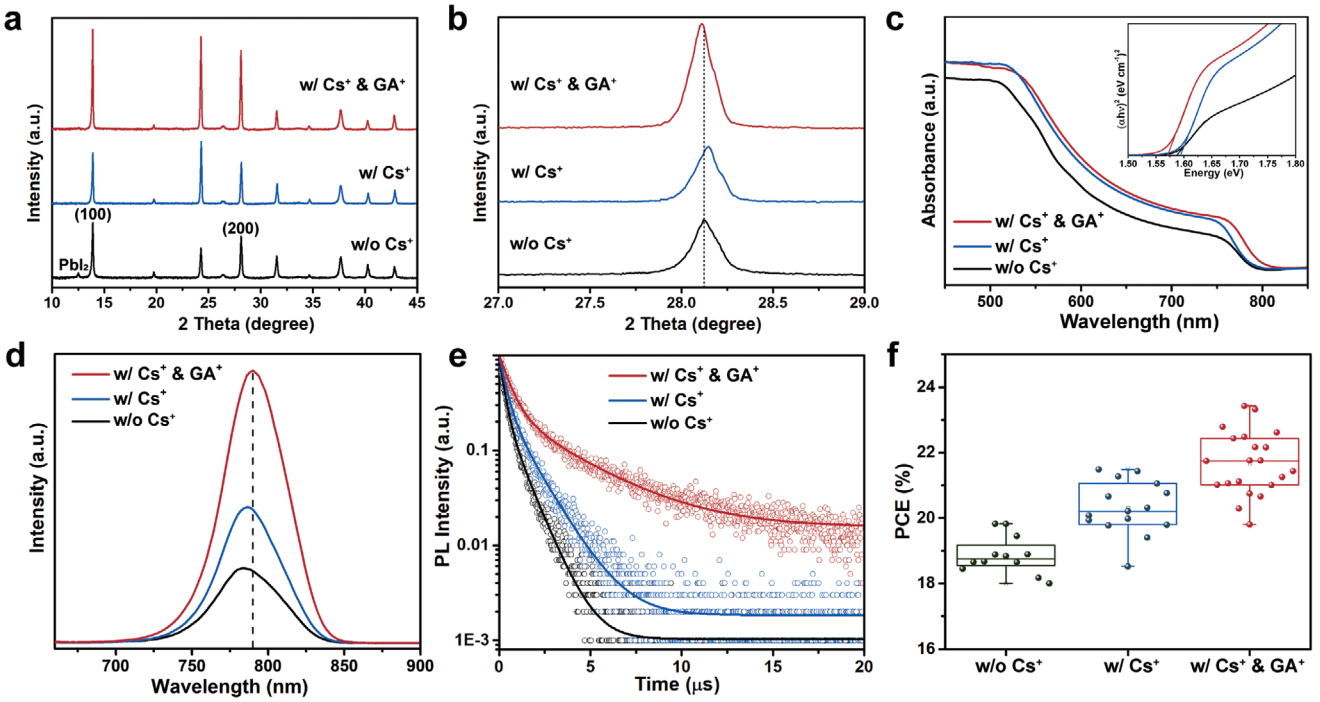

Figure 5. Ex situ film characterizations. a) Ex situ XRD spectra and b) the enlarged spectra in a Two Theta range between 27° and 29° of perovskite films without Cs^+ doping, with 5% Cs^+, and with 5% Cs^+ and 4 mg mL^{-1} GA^+. c) The absorption spectra and Tauc plots. d) The steady-state PL and e) TRPL spectra of perovskite films deposited on glasses. f) Statistical device performance based on different perovskite films.

of FA^+. On the contrary, the incorporation of GA^+ compensates the weak bonding induced by Cs^+. In the crystallization process of the perovskite (reaction 2), GA^+ ions together with FA^+ ions can relax the lattice strain in the perovskites, which is created by small Cs^+ cations, and thereby form stronger bonds with surrounding Pb–I inorganic frameworks.[13,37,38] In addition, we employed the Williamson–Hall method to calculate the lattice strain from GIWAXS results (Figure 3). The breadth of scattering peaks at different scattering angles are fitted with the equation $\beta\cos\theta = \frac{K\lambda}{D} + 4\varepsilon\sin\theta$, where β is the integral breadth, θ is the scattering angle, K is a shape factor (in this case 0.9) λ is the wavelength, D is the volume-weighted mean domain size, and ε is the lattice strain.[39] The Williamson–Hall plots of different perovskite films are presented in Figure S13 in the Supporting Information, showing that the lattice strain is increased with the incorporation of Cs^+ but relaxed after doping with GA^+, which agrees with the DFT calculations. The relaxed lattice strain and stronger bonds facilitate a more rapid phase transition from the δ-$CsPbI_3$ to the perovskite phase in the film with Cs^+ & GA^+ (Figure 3i).

To understand the underlying reasons for the formation and elimination of pinholes caused by Cs^+ and GA^+, respectively, a schematics of the classical Gibbs free energy diagram are shown in Figure S14 in the Supporting Information based on the thermodynamic process of nucleation.[40] The total free energy (ΔG) is composed of the surface free energy (ΔG_s) and the bulk free energy (ΔG_v), while it can be also determined by the equation of $\Delta G = \Delta H - T\Delta S$. The perovskite crystallization process is triggered by the formation of perovskite nuclei, serving as a template for the growth of perovskite crystals. For a stable nucleation process, a critical free energy (ΔG^*) is required to be overcome, as illustrated in Figure S14a in the Supporting Information. Based on the DFT calculation results, the nucleation in the film with Cs^+ occurs from the δ-$CsPbI_3$ has a lower enthalpy (ΔH), and hence a lower ΔG^* (Figure S14b, Supporting Information), which further confirms the nucleation prefers to initiate at the δ-$CsPbI_3$ phase instead of the PbI_2 phase. Meanwhile, we found that the PbI_2 film with Cs^+ shows a smoother surface than the counterpart without Cs^+ (Figure S15, Supporting Information), which may also give rise to fewer nucleation sites in the film with Cs^+.[41] It is noted that uniform nucleation and growth are very important to obtain a flat and smooth film without pinholes.[42] However, the film with Cs^+ offers sparse nucleation centers that are mainly originated from the sparse δ-$CsPbI_3$ crystals (Figure S15c,d, Supporting Information), resulting in nonuniform nucleation and appearance of pinholes. Fortunately, incorporating GA^+ in the second step can eliminate pinholes induced by Cs^+. It is reported that the grain density (N) is determined by the equation of $N = 1.1\left(\frac{V_1}{V_2}\right)^{0.5}$,[43] where V_1 and V_2 are the nucleation rate and growth rate, respectively. According to the GIWAXS results (Figure 4e) and DFT calculations (Figure 4g), the growth rate (V_2) is increased by the incorporation of GA^+, resulting in a lower grain density and thus a larger grain size. Therefore, the pinholes can be suppressed via the effective Ostwald ripening process and enhanced grain boundary migration.[44]

To correlate the diverse crystallization pathways with film properties, we carried out a series of ex situ characterizations for the perovskite films without doping, with Cs^+, and with Cs^+ & GA^+. The perovskite film with Cs^+ & GA^+ shows

© 2020 Wiley-VCH GmbH

the highest XRD peak intensity and the smallest full width at half maximum (FWHM), as shown in **Figure 5**a and Figure S16 in the Supporting Information, indicating a higher crystallinity and a longer coherence length. The (200) peak shifts to a slightly larger scattering angle (2θ) with the Cs^+ doping and back to a smaller 2θ with both Cs^+ and GA^+ (Figure 5b), demonstrating the respective lattice contraction and expansion caused by the incorporation of Cs^+ and GA^+ into the perovskite crystal lattice.[37] More detailed XRD results of the films with different concentrations of Cs^+ and GA^+ doping are included in Figures S17 and S12 in the Supporting Information, respectively. The remnant PbI_2 peak in the perovskite films is eliminated with a higher Cs^+ concentration of 5% or 10%, while a higher concentration of GA^+ can deliver a better crystallinity for the perovskite films with Cs^+ & GA^+. It is noted that the low-dimensional GA-related phases are not detected in the film with Cs^+ & GA^+ due to a relatively lower concentration of GA^+ in the film (<10%),[13,37] while the film formed from the PbI_2 and pure GAI (100%) will lead to the formation of $GAPbI_3$ and GA_2PbI_4,[45] as shown in Figure S18 in the Supporting Information. Figure 5c shows the absorption spectra of different perovskite films, and the film with Cs^+ & GA^+ exhibits a relatively smaller optical bandgap calculated from Tauc plots. Previous studies reported that adding GA^+ into $MAPbI_3$ caused a slight increase of optical bandgap,[13] which was later ascribed to the tilting and distortion of the octahedra in the Pb–I inorganic framework after incorporating GA^+.[46] In the current case, the addition of GA^+ relaxes the local lattice strain created by small Cs^+ cations as indicated by DFT results (Figure 4g), thus slightly reducing the bandgap. In addition, trap-induced recombination in the perovskite films is investigated by steady-state photoluminescence (PL) and time-resolved photoluminescence (TRPL) measurements. In Figure 5d, the PL emission intensity of the perovskite film increases after Cs^+ doping in compared to the undoped film, which might be ascribed to the overall larger grain size, despite the presence of pinholes. As expected, the emission intensity is further enhanced with the addition of GA^+, owing to the largest grain size, as well as to the pinhole-free film morphology. Besides the increased intensity, a slight redshift of the PL was observed in the perovskite film with Cs^+ & GA^+, which is consistent with the observed smaller optical bandgap. Fewer traps in the perovskite film with Cs^+ & GA^+ were further confirmed by TRPL shown in Figure 5e and Table S3 in the Supporting Information. The average carrier lifetime for perovskite without doping, with Cs^+, and with Cs^+ & GA^+ are 651, 962, and 2426 ns, respectively. The higher PL intensity and longer lifetime of the perovskite film with Cs^+ & GA^+ are in accordance with the better film morphology (Figure 4d) and the higher crystallinity (Figure 5a). The defect densities of different perovskite films are also evaluated by the space-charge-limited current (SCLC) measurements with the device structure of FTO/SnO_2/perovskite/[6,6]-phenyl-C_{71}-butyric acid methyl ester/Au,[47] as shown in Figure S19 in the Supporting Information. The defect density (N_t) is determined by the equation of $N_t = \frac{2\varepsilon_r\varepsilon_0 V_{TFL}}{qL^2}$, where ε_r is the relative dielectric constant,[48] ε_0 is the vacuum permittivity, V_{TFL} is the onset voltage of the trap-filled limit region, q is the elementary charge, and L is the thickness of the film. The defect density of the perovskite films without Cs^+, with Cs^+, and with Cs^+ & GA^+ is calculated to be 1.35×10^{16}, 7.01×10^{15}, and 3.10×10^{15} cm^{-3}, respectively, which confirms that the perovskite with Cs^+ & GA^+ exhibits a reduced defect density.

To understand the influence of the sequential doping to the device performance, photovoltaic devices are fabricated based on perovskite films without doping, with Cs^+, and with Cs^+ & GA^+. Figure S20a in the Supporting Information shows the cross-sectional SEM image of a typical device with the structure of FTO/SnO_2/perovskite/spiro-OMeTAD/Au. Device performance statistics based on these perovskite films are summarized in Figure 5f and Figure S20 in the Supporting Information. The PSCs without Cs^+ deliver an average efficiency of 18.86% with an open-circuit voltage (V_{OC}) of 1.12 V, a short circuit current (J_{SC}) of 23.93 mA cm^{-2}, and a fill factor (FF) of 0.703. In contrast, the devices with Cs^+ suffer an obvious V_{OC} drop, which agrees with the existence of pinholes that causes severe carrier recombination.[2] The V_{OC} of the ideal solar cell can be calculated by the equation of $V_{oc} = \frac{k_B T}{q} \ln\left(\frac{J_{ph}}{J_0} + 1\right)$, where q is the elementary charge, k_B is the Boltzmann constant, T is the temperature, J_{ph} is the photogenerated current density, and J_0 is the saturation current density, which depends on the recombination in the solar cell. Based on the equation, more recombination will lead to a higher saturation current density J_0, thus reducing the V_{OC}. Nonetheless, the fill factor and J_{SC} are still enhanced with Cs^+ doping, benefiting from the enhanced light absorption in the full range of 450–770 nm (Figure 5c), lower defect density due to the overall larger grain size of the perovskite film with Cs^+ (Figure S10, Supporting Information), and the higher crystallinity (Figures S16 and S17, Supporting Information). The addition of GA^+ in the perovskite with Cs^+ further pushes the average PCE to 21.67%. Despite a smaller optical bandgap (Figure 5c), a higher average V_{OC} of 1.13 V is obtained for the film with Cs^+ & GA^+. It is ascribed to the eliminated pinholes in the film, thus significantly suppressing the trap-induced recombination, effectively reducing the V_{OC} loss[14,49] and contributing to a better FF. J–V curves of typical devices based on the perovskite films without Cs^+, with Cs^+, and with Cs^+ & GA^+ measured from both reverse and forward scanning directions, external quantum efficiency (EQE), and steady-state outputs are shown in Figure S21 in the Supporting Information. The variation in the device performance with respect to the concentration of Cs^+ and GA^+ is summarized in Figures S22 and S23 in the Supporting Information. The champion device with 5% Cs^+ and 4 mg mL^{-1} GA^+ has a PCE of 23.5% with a V_{OC} of 1.16 V, J_{SC} of 24.8 mA cm^{-2}, and a FF of 0.813. The J–V characteristics are shown in Figure S24 in the Supporting Information. In addition, the unencapsulated devices based on the perovskite films with Cs^+ & GA^+ demonstrate a better long-term stability under both the dark and light conditions (Figure S25, Supporting Information).

In summary, we have systematically studied the complete crystallization pathways of a benchmark $FAPbI_3$-based perovskite and the influence of sequential doping of A-site cations of Cs^+ in the first step and GA^+ in the second step. In the light of in situ GIWAXS results, three distinct crystallization pathways have been identified: a direct phase transition from PbI_2 to perovskites for the film without doping, an alternative phase

© 2020 Wiley-VCH GmbH

transition from δ-$CsPbI_3$ to perovskites and a relatively faster phase transition from δ-$CsPbI_3$ to perovskites with the assistance of GA^+. Interestingly, the diverse crystallization pathways lead to markedly distinct film morphologies due to the different film-formation kinetics. The doping of Cs^+ cations in the first step promotes the formation of the δ-$CsPbI_3$ phase and suppresses the formation of the hexagonal PbI_2 phase, which provides more favorable and fewer nucleation sites. The favorability corresponds to the enthalpy of the reaction from δ-$CsPbI_3$ to perovskite being lower than that of the reaction directly from PbI_2 to perovskite. However, the sparse nucleation sites of δ-$CsPbI_3$ lead to many unexpected pinholes. Fortunately, introducing GA^+ cations in the second step solves this problem via Ostwald ripening and enhanced grain boundary migration. Besides, the crystal growth of perovskites is also accelerated by GA^+, which correlates with a larger bonding strength between the GA^+ and the lead-halide octahedral framework and a more stable ternary (GACsFA) phase. These perovskite films exhibit a higher crystallinity and reduced defect density, due to the synergistic effects of Cs^+ and GA^+. Efficient PSCs with high PCEs of over 23% have been achieved.

We find that the two-step process can effectively decouple the crystal nucleation and growth into two steps, providing precise control handles for perovskite film growth. However, for the one-step process, perovskite nucleation and crystal growth are occurring together. It is challenging to optimize these two aspects separately. Our work demonstrates the feasibility of fine-tuning the crystallization pathways using sequential A-site doping in the two-step fabrication. Future research on sequential X-site (e.g., I^-, Br^-, Cl^-) or M-site (e.g., Pb^{2+}, Sn^{2+}, Ge^{2+}) doping to optimize the nucleation and crystal growth for the design of novel fabrication recipes toward high-efficiency PSCs is worth further exploration.

Experimental Section

Materials: FTO glass and spiro-OMeTAD were purchased from Advanced Election Technology Co., Ltd; $SnCl_2$ (99%) was purchased from Aladdin; lead iodide (99.999%) was purchased from Xi'an Polymer Light Technology Corp.; FAI, MABr, and MACl were purchased from Greatcell Solar; GAI was purchased from TCI. All the other chemical materials were purchased from Sigma-Aldrich and used as received unless stated otherwise.

Device Fabrication: FTO substrates were sequentially rinsed by sonication in detergent, deionized (DI) water, acetone, and isopropanol for 30 min, respectively, and then dried under nitrogen gas. Cleaned FTO substrates were treated with ultraviolet-ozone for 15 min, followed by deposition of a SnO_2 electron transporting layer on the substrate by spin-coating the colloidal SnO_2 nanoparticle solution at 3000 rpm for 30 s, and subsequently annealed at 200 °C for 60 min on a hotplate. The colloidal SnO_2 precursor solution was prepared by mixing $SnCl_2$ and CH_4N_2S with a mass ratio of 3:1 in 30 mL DI water; the mixture was stirred for 1–2 d until the solution turned to yellow and clear. The perovskite layer was fabricated in the glovebox through a modified two-step sequential method according to the literature. First, 1.3 M PbI_2 precursor, which was dissolved in a mixture of DMF/DMSO with the volume ratio of 95:5, was spin-coated on the SnO_2/FTO substrate at 1500 rpm for 30 s, and dried at 70 °C for 1 min. Different amounts of CsI solution (1.5 M in DMSO) were added to the PbI_2 precursor to obtain the desired Cs^+ concentration. Thereafter, a mixture solution of FAI:MABr:MACl:GAI (60 mg:6 mg:6 mg:*x* mg in 1 mL IPA, *x* is from 0 to 8 mg) was dropped on the PbI_2 film at 1500 rpm for 30 s. The as-cast perovskite film was annealed at 100 °C for 20 min. The spiro-OMeTAD solution was composed of 72.3 mg spiro-OMeTAD, 28.8 µL TBP, and 17.5 µL Li-TFSI solution (520 mg in 1 mL acetonitrile) in 1 mL chlorobenzene, and then spin-coated on perovskite film at 4000 rpm for 30 s. Finally, a 60 nm Au electrode was deposited by thermal evaporation.

In Situ GIWAXS Experiments: GIWAXS measurements were conducted at the 23A small- and wide-angle X-ray scattering (SWAXS) beamline of the Taiwan Light Source at the NSRRC, Hsinchu, Taiwan.[20] The wavelength of the X-rays was 1.240 Å (10 keV) and the scattering signals were collected by a C9728DK area detector, which was placed at ≈169 mm distance from the sample. The sample-to-detector distance was calibrated with a lanthanum hexaboride (LaB_6) sample. The spin-coating and annealing procedures were conducted using a custom-built spin-coater chamber and a remotely controlled hotplate chamber, respectively.[50] Both chambers were air-tight and filled with N_2 during the experiment. The incident angle was kept at 2° to enhance the signal resolution with a frame exposure time of 1 or 2 s. In the first step, the PbI_2 precursor was dropped on the substrate in advance, and the GIWAXS measurement and sample spinning were triggered simultaneously. In the second step, a certain amount of IPA solution containing organic salts was injected on the PbI_2 film through a motorized syringe, and the whole process was monitored with GIWAXS. The spin speed of both two steps was kept at 1500 rpm, which is the same value as in the device fabrication procedure. There was no visible evidence of X-ray damage on the sample after measurements.

Characterizations: The surface morphology of PbI_2 and perovskite films was characterized by high-resolution field emission scanning electron microscopy (HR-FESEM) (FEI, Quanta 400). The crystalline structures for the perovskite films were measured by XRD on a Rigaku Smart Lab (λ = 1.54 Å). UV–vis absorption spectra were taken on a Hitachi U-3501 ultraviolet/visible/near-infrared spectrophotometer. The current density–voltage (*J*–*V*) curves were characterized by a Keithley B2901A source meter unit under an AM 1.5G solar simulator (100 mW cm^{-2}). The devices were measured without pretest illumination and bias poling, and the scan rate was 0.2 V s^{-1}. Photoluminescence measurements of perovskite films on glass were conducted by using an Edinburgh FLSP920 spectrophotometer installed with an excitation source of 485 nm picosecond pulsed diode laser with an average power of 0.15 mW.

DFT Calculations: All calculations were performed using DFT[51] and the projector-augmented wave (PAW) technique, as implemented in the Vienna ab initio simulation package (VASP).[52] The generalized gradient approximation (GGA) with the Perdew–Burke–Ernzerhof (PBE) exchange–correlation functional was used.[53] The cell volume and positions of the ions were fully relaxed during geometry optimization. An energy cutoff of 500 eV and 2 × 2 × 1 *k*-point meshes were used. The energy and force convergence criteria were set to 10^{-5} eV and 5 meV $Å^{-1}$, respectively. Spin–orbit coupling (SOC) was included in the self-consistent calculations based on the equilibrium structures.[54] For simulations of complex perovskite alloys, a 2 × 2 × 4 supercell of $FAPbI_3$ perovskite (based on a cubic primitive cell with lattice parameter *a* = 6.45 Å) was used as a starting structure, where different structures were created by replacing one FA^+ cation and/or three I^- anions by one GA^+ and/or one Cs^+ cation and three Br^- anions, respectively. So, the concentrations of Cs^+, GA^+, and Br^- were 6.25% for each, respectively, which closely matched the experimental concentrations, i.e., 5.5–6% of Cs^+, ≈6.47% of GA^+, and ≈5% of Br^-. The special relative positions of these three incorporated ions were adopted from the previous work,[37] where three Br^- anions form one facet of an octahedron that pulls the nearby Cs^+ cation away from its A site, leaving sufficient room in the opposite diagonal direction for the nearby GA^+ cation. Then, the most stable structures of all relevant perovskites were selected after testing dozens of configurations. Details of all configurations are given in Table S4 in the Supporting Information. The density derived electrostatic and chemical (DDEC6) method[55] was used to calculate the total bond order of chemical bonds associated with the interaction of the FA^+, Cs^+, or GA^+ cations with the surrounding Pb and I atoms.

© 2020 Wiley-VCH GmbH

Supporting Information

Supporting Information is available from the Wiley Online Library or from the author.

Acknowledgements

M.Q. and H.X. contributed equally to this work. The authors are grateful for the beam time and technical supports provided by 23A SWAXS beamline at NSRRC, Hsinchu. The authors acknowledge the financial support from the Research Grant Council of Hong Kong (RGC) (General Research Fund No. 14314216). H.X. acknowledges the funding from the China Scholarship Council (CSC). S.T. acknowledges funding by the Computational Sciences for Energy Research (CSER) tenure track program of Shell and NWO (Project number 15CST04-2), The Netherlands. G.L. thanks funding from RGC (CRF Group Research Grant C5037-18G).

Conflict of Interest

The authors declare no conflict of interest.

Keywords

crystallization kinetics, perovskite solar cells, reaction enthalpy, sequential A-site doping, two-step method

Received: July 7, 2020
Revised: August 7, 2020
Published online: September 16, 2020

[1] Best Research-Cell Efficiency Chart from NREL, https://www.nrel.gov/pv/cell-efficiency.html (accessed: July 2020).
[2] J. Chen, N. G. Park, *Adv. Mater.* **2019**, *31*, 1803019.
[3] M. Ahmadi, T. Wu, B. Hu, *Adv. Mater.* **2017**, *29*, 1605242.
[4] N. Ahn, D. Y. Son, I. H. Jang, S. M. Kang, M. Choi, N. G. Park, *J. Am. Chem. Soc.* **2015**, *137*, 8696.
[5] N. J. Jeon, J. H. Noh, W. S. Yang, Y. C. Kim, S. Ryu, J. Seo, S. I. Seok, *Nature* **2015**, *517*, 476.
[6] W. S. Yang, J. H. Noh, N. J. Jeon, Y. C. Kim, S. Ryu, J. Seo, S. I. Seok, *Science* **2015**, *348*, 1234.
[7] A. Kojima, K. Teshima, Y. Shirai, T. Miyasaka, *J. Am. Chem. Soc.* **2009**, *131*, 6050.
[8] Z. Xiao, C. Bi, Y. Shao, Q. Dong, Q. Wang, Y. Yuan, C. Wang, Y. Gao, J. Huang, *Energy Environ. Sci.* **2014**, *7*, 2619.
[9] J. H. Im, I. H. Jang, N. Pellet, M. Gratzel, N. G. Park, *Nat. Nanotechnol.* **2014**, *9*, 927.
[10] M. Xiao, F. Huang, W. Huang, Y. Dkhissi, Y. Zhu, J. Etheridge, A. Gray-Weale, U. Bach, Y. B. Cheng, L. Spiccia, *Angew. Chem.* **2014**, *53*, 9898.
[11] N. J. Jeon, J. H. Noh, Y. C. Kim, W. S. Yang, S. Ryu, S. I. Seok, *Nat. Mater.* **2014**, *13*, 897.
[12] a) M. Saliba, T. Matsui, J. Y. Seo, K. Domanski, J. P. Correa-Baena, M. K. Nazeeruddin, S. M. Zakeeruddin, W. Tress, A. Abate, A. Hagfeldt, M. Gratzel, *Energy Environ. Sci.* **2016**, *9*, 1989; b) M. Saliba, T. Matsui, K. Domanski, J. Y. Seo, A. Ummadisingu, S. M. Zakeeruddin, J. P. Correa-Baena, W. R. Tress, A. Abate, A. Hagfeldt, M. Gratzel, *Science* **2016**, *354*, 206; c) N. J. Jeon, H. Na, E. H. Jung, T.-Y. Yang, Y. G. Lee, G. Kim, H.-W. Shin, S. Il Seok, J. Lee, J. Seo, *Nat. Energy* **2018**, *3*, 682; d) E. H. Jung, N. J. Jeon, E. Y. Park, C. S. Moon, T. J. Shin, T.-Y. Yang, J. H. Noh, J. Seo, *Nature* **2019**, *567*, 511.
[13] A. D. Jodlowski, C. Roldán-Carmona, G. Grancini, M. Salado, M. Ralaiarisoa, S. Ahmad, N. Koch, L. Camacho, G. de Miguel, M. K. Nazeeruddin, *Nat. Energy* **2017**, *2*, 972.
[14] D. Luo, W. Yang, Z. Wang, A. Sadhanala, Q. Hu, R. Su, R. Shivanna, G. F. Trindade, J. F. Watts, Z. Xu, T. Liu, K. Chen, F. Ye, P. Wu, L. Zhao, J. Wu, Y. Tu, Y. Zhang, X. Yang, W. Zhang, R. H. Friend, Q. Gong, H. J. Snaith, R. Zhu, *Science* **2018**, *360*, 1442.
[15] Q. Jiang, Y. Zhao, X. Zhang, X. Yang, Y. Chen, Z. Chu, Q. Ye, X. Li, Z. Yin, J. You, *Nat. Photonics* **2019**, *13*, 460.
[16] Q. Jiang, L. Zhang, H. Wang, X. Yang, J. Meng, H. Liu, Z. Yin, J. Wu, X. Zhang, J. You, *Nat. Energy* **2017**, *2*, 16177.
[17] C. Y. Lin, S. S. Li, J. W. Chang, H. C. Chia, Y. Y. Hsiao, C. J. Su, B. J. Lian, C. Y. Wen, S. K. Huang, W. R. Wu, D. Y. Wang, A. C. Su, C. W. Chen, U. S. Jeng, *Adv. Funct. Mater.* **2019**, *29*, 1902582.
[18] a) B. Dou, V. L. Pool, M. F. Toney, M. F. A. M. van Hest, *Chem. Mater.* **2017**, *29*, 5931; b) V. L. Pool, B. Dou, D. G. Van Campen, T. R. Klein-Stockert, F. S. Barnes, S. E. Shaheen, M. I. Ahmad, M. F. A. M. van Hest, M. F. Toney, *Nat. Commun.* **2017**, *8*, 4960.
[19] R. Munir, A. D. Sheikh, M. Abdelsamie, H. Hu, L. Yu, K. Zhao, T. Kim, O. E. Tall, R. Li, D. M. Smilgies, A. Amassian, *Adv. Mater.* **2017**, *29*, 1604113.
[20] M. Qin, K. Tse, T. K. Lau, Y. Li, C. J. Su, G. Yang, J. Chen, J. Zhu, U. S. Jeng, G. Li, H. Chen, X. Lu, *Adv. Mater.* **2019**, *31*, 1901284.
[21] Y. Fan, J. Fang, X. Chang, M.-C. Tang, D. Barrit, Z. Xu, Z. Jiang, J. Wen, H. Zhao, T. Niu, D.-M. Smilgies, S. Jin, Z. Liu, E. Q. Li, A. Amassian, S. Liu, K. Zhao, *Joule* **2019**, *3*, 2485.
[22] Q. Hu, L. Zhao, J. Wu, K. Gao, D. Luo, Y. Jiang, Z. Zhang, C. Zhu, E. Schaible, A. Hexemer, C. Wang, Y. Liu, W. Zhang, M. Gratzel, F. Liu, T. P. Russell, R. Zhu, Q. Gong, *Nat. Commun.* **2017**, *8*, 15688.
[23] P. Gratia, I. Zimmermann, P. Schouwink, J. H. Yum, J. N. Audinot, K. Sivula, T. Wirtz, M. K. Nazeeruddin, *ACS Energy Lett.* **2017**, *2*, 2686.
[24] M. Saliba, J.-P. Correa-Baena, C. M. Wolff, M. Stolterfoht, N. Phung, S. Albrecht, D. Neher, A. Abate, *Chem. Mater.* **2018**, *30*, 4193.
[25] J. Bing, S. Huang, A. W. Y. Ho-Baillie, *Energy Technol.* **2020**, *8*, 1901114.
[26] Q. Jiang, Z. Chu, P. Wang, X. Yang, H. Liu, Y. Wang, Z. Yin, J. Wu, X. Zhang, J. You, *Adv. Mater.* **2017**, *29*, 1703852.
[27] K. Meng, X. Wang, Q. Xu, Z. Li, Z. Liu, L. Wu, Y. Hu, N. Liu, G. Chen, *Adv. Funct. Mater.* **2019**, *29*, 1902319.
[28] a) A. Wakamiya, M. Endo, T. Sasamori, N. Tokitoh, Y. Ogomi, S. Hayase, Y. Murata, *Chem. Lett.* **2014**, *43*, 711; b) M. V. Lee, S. R. Raga, Y. Kato, M. R. Leyden, L. K. Ono, S. Wang, Y. Qi, *J. Mater. Res.* **2017**, *32*, 45.
[29] X. Liu, S. T. Ha, Q. Zhang, M. de la Mata, C. Magen, J. Arbiol, T. C. Sum, Q. Xiong, *ACS Nano* **2015**, *9*, 687.
[30] a) Q. Ye, Y. Zhao, S. Mu, F. Ma, F. Gao, Z. Chu, Z. Yin, P. Gao, X. Zhang, J. You, *Adv. Mater.* **2019**, *31*, 1905143; b) Q. Zeng, X. Zhang, X. Feng, S. Lu, Z. Chen, X. Yong, S. A. T. Redfern, H. Wei, H. Wang, H. Shen, W. Zhang, W. Zheng, H. Zhang, J. S. Tse, B. Yang, *Adv. Mater.* **2018**, *30*, 1705393.
[31] J. A. Steele, H. Jin, I. Dovgaliuk, R. F. Berger, T. Braeckevelt, H. Yuan, C. Martin, E. Solano, K. Lejaeghere, S. M. J. Rogge, C. Notebaert, W. Vandezande, K. P. F. Janssen, B. Goderis, E. Debroye, Y.-K. Wang, Y. Dong, D. Ma, M. Saidaminov, H. Tan, Z. Lu, V. Dyadkin, D. Chernyshov, V. Van Speybroeck, E. H. Sargent, J. Hofkens, M. B. J. Roeffaers, *Science* **2019**, *365*, 679.
[32] a) Y. Guo, K. Shoyama, W. Sato, Y. Matsuo, K. Inoue, K. Harano, C. Liu, H. Tanaka, E. Nakamura, *J. Am. Chem. Soc.* **2015**, *137*, 15907; b) J. Cao, X. J. Jing, J. Z. Yan, C. Y. Hu, R. H. Chen, J. Yin, J. Li, N. F. Zheng, *J. Am. Chem. Soc.* **2016**, *138*, 9919.
[33] A. A. Petrov, I. P. Sokolova, N. A. Belich, G. S. Peters, P. V. Dorovatovskii, Y. V. Zubavichus, V. N. Khrustalev, A. V. Petrov,

 © 2020 Wiley-VCH GmbH

M. Grätzel, E. A. Goodilin, A. B. Tarasov, *J. Phys. Chem. C* **2017**, *121*, 20739.
[34] C. Li, Q. Guo, H. Zhang, Y. Bai, F. Wang, L. Liu, T. Hayat, A. Alsaedi, Z. Tan, *Nano Energy* **2017**, *40*, 248.
[35] a) J. N. Bronsted, *Chem. Rev.* **1928**, *5*, 231; b) M. G. Evans, M. Polanyi, *Trans. Faraday Soc.* **1938**, *34*, 11.
[36] J. Jiang, C. K. Onwudinanti, R. A. Hatton, P. A. Bobbert, S. Tao, *J. Phys. Chem. C* **2018**, *122*, 17660.
[37] Y. Zhou, H. Xue, Y. H. Jia, G. Brocks, S. Tao, N. Zhao, *Adv. Funct. Mater.* **2019**, *29*, 1905739.
[38] J. Ma, M. Qin, Y. Li, T. Zhang, J. Xu, G. Fang, X. Lu, *J. Mater. Chem. A* **2019**, *7*, 27640.
[39] a) G. K. Williamson, W. H. Hall, *Acta Metall.* **1953**, *1*, 22; b) K. Nishimura, D. Hirotani, M. A. Kamarudin, Q. Shen, T. Toyoda, S. Iikubo, T. Minemoto, K. Yoshino, S. Hayase, *ACS Appl. Mater. Interfaces* **2019**, *11*, 31105.
[40] N. T. K. Thanh, N. Maclean, S. Mahiddine, *Chem. Rev.* **2014**, *114*, 7610.
[41] a) Y. Li, B. Ding, Q.-Q. Chu, G.-J. Yang, M. Wang, C.-X. Li, C.-J. Li, *Sci. Rep.* **2017**, *7*, 46141; b) L. Gao, G. Yang, *Sol. RRL* **2020**, *4*, 1900200.
[42] D. Liu, W. Zhou, H. Tang, P. Fu, Z. Ning, *Sci. China: Chem.* **2018**, *61*, 1278.
[43] a) L. Li, Y. Chen, Z. Liu, Q. Chen, X. Wang, H. Zhou, *Adv. Mater.* **2016**, *28*, 9862; b) H. Hu, M. Singh, X. Wan, J. Tang, C.-W. Chu, G. Li, *J. Mater. Chem. A* **2020**, *8*, 1578.
[44] a) N. D. Pham, V. T. Tiong, D. Yao, W. Martens, A. Guerrero, J. Bisquert, H. Wang, *Nano Energy* **2017**, *41*, 476. b) S. Xiao, Y. Bai, X. Meng, T. Zhang, H. Chen, X. Zheng, C. Hu, Y. Qu, S. Yang, *Adv. Funct. Mater.* **2017**, *27*, 1604944.
[45] A. D. Jodlowski, A. Yépez, R. Luque, L. Camacho, G. de Miguel, *Angew. Chem., Int. Ed.* **2016**, *55*, 14972.
[46] S. Tao, I. Schmidt, G. Brocks, J. Jiang, I. Tranca, K. Meerholz, S. Olthof, *Nat. Commun.* **2019**, *10*, 2560.
[47] a) T. Niu, J. Lu, X. Jia, Z. Xu, M. C. Tang, D. Barrit, N. Yuan, J. Ding, X. Zhang, Y. Fan, T. Luo, Y. Zhang, D. M. Smilgies, Z. Liu, A. Amassian, S. Jin, K. Zhao, S. Liu, *Nano Lett.* **2019**, *19*, 7181; b) T. Zhang, L. Xie, L. Chen, N. Guo, G. Li, Z. Tian, B. Mao, Y. Zhao, *Adv. Funct. Mater.* **2017**, *27*, 1603568.
[48] D. Barrit, P. Cheng, K. Darabi, M.-C. Tang, D.-M. Smilgies, S. Liu, T. D. Anthopoulos, K. Zhao, A. Amassian, *Adv. Funct. Mater.* **2020**, *30*, 1907442.
[49] S. Zhao, J. Xie, G. Cheng, Y. Xiang, H. Zhu, W. Guo, H. Wang, M. Qin, X. Lu, J. Qu, J. Wang, J. Xu, K. Yan, *Small* **2018**, *14*, 1803350.
[50] W.-R. Wu, C.-J. Su, W.-T. Chuang, Y.-C. Huang, P.-W. Yang, P.-C. Lin, C.-Y. Chen, T.-Y. Yang, A.-C. Su, K.-H. Wei, C.-M. Liu, U. S. Jeng, *Adv. Energy Mater.* **2017**, *7*, 1601842.
[51] W. Kohn, L. J. Sham, *Phys. Rev.* **1965**, *140*, A1133.
[52] a) G. Kresse, J. Furthmüller, *Comput. Mater. Sci.* **1996**, *6*, 15; b) G. Kresse, J. Furthmüller, *Phys. Rev. B* **1996**, *54*, 11169.
[53] J. P. Perdew, K. Burke, M. Ernzerhof, *Phys. Rev. Lett.* **1996**, *77*, 3865.
[54] J. Even, L. Pedesseau, J.-M. Jancu, C. Katan, *J. Phys. Chem.* **2013**, *4*, 2999.
[55] a) T. A. Manz, N. G. Limas, *RSC Adv.* **2016**, *6*, 47771; b) N. G. Limas, T. A. Manz, *RSC Adv.* **2016**, *6*, 45727.

© 2020 Wiley-VCH GmbH